0254-6124/2018/38(5)-598–06 *Chin. J. Space Sci.* 空间科学学报

XU Lin, ZOU Yongliao, QIN Lang. Latest scientific results of China's Lunar Exploration Program. *Chin. J. Space Sci.*, 2018, **38**(5): 598-603. DOI:10.11728/cjss2018.05.598

Latest Scientific Results of China's Lunar Exploration Program*

XU Lin[1] ZOU Yongliao[1] QIN Lang[1,2]

1(*State Key Laboratory of Space Weather, National Space Science Center, Chinese Academy of Sciences, Beijing* 100190)

2(*University of Chinese Academy of Sciences, Beijing* 100049)

Abstract Through the implementation of China's Lunar Exploration Program (CLEP), a large amount of data has been acquired. This paper will present the latest scientific results based on these data involving the composition, topography, space environment, subsurface structure of the Moon, and asteroid exploration and moon-based observations, *etc.*

Key words CLEP, Lunar geology, Microwave mapping, Subsurface structure, Impact crater, Asteroid Toutatis

Classified index V 4, P 3

1 Introduction

Upto now, China has successfully launched Chang'E-1 (CE-1), Chang'E-2 (CE-2) and Chang'E-3 (CE-3) spacecraft. The Chang'E-1 spacecraft is an orbiter, carrying 8 scientific instruments working in the 200 km high orbit more than 1 year. As a backup to Chang'E-1, Chang'E-2 orbiter was launched on October 1, 2010, and successfully entered the working orbit of 100 km above the lunar surface and obtained the images of topography with a resolution of 1.3 m of the landing site for Chang'E-3. And then, Chang'E-2 spacecraft conducted an extended mission, especially with the close flyby of the 4179 asteroid Toutatis and obtained a 10 m-resolution image. The Chang'E-3 spacecraft consists of a lander and a rover (named as Yutu), which was launched on December 2, 2013, successfully soft-landed and patrolled.

Through the implementation of these missions, many scientific results have been obtained by analyzing these data from the CLEP involving the chemical composition, soil temperature of lunar surface, near-lunar space environment, shallow structural characteristics and the geological history of the Imbrium basin, the Earth's plasmasphere in a global scale meridian view by the Extreme Ultra-Violet (EUV) camera, and monitoring variable stars, bright active galactic nuclei by a moon-based Lunar Ultraviolet Telescope (LUT). These results help us to understand more about the formation and evolution of the Moon.

This paper mainly introduces the scientific results published between 2016 and 2017 based on these data, and the technical results are not included. In addition, because there are too many contents involved, this article cannot cover all, and only a few representative ones are introduced.

2 Lunar Science

2.1 Composition and Magmatism

Ferroan anorthosite, magnesian suite, alkali suite, KREEP basalt and mare basalt are five primary lunar rock types. Wang *et al.*[1] mapped the thorium distribution of global Moon with the data of Chang'E-2 Gamma-Ray Spectrometer (GRS). And a symmetrical layout along the two sides of the high-Th annular belt was found in the Procellarum KREEP Terrane (PKT). The ring-like high-Th belt may be formed by KREEP basaltic volcanism rather than by Imbrium impact. Besides, Wang *et al.*[2] also reported a new lithologic distribution map across the Moon (Figure 1)[2]. A new geochemical index termed with the abundance ratios of various oxides and elements was proposed firstly in the study. And then, the

* Supported by National Science Foundation of China (41590851)
Received 11 June 2018
E-mail: xulin@nssc.ac.cn

Moon was classified and mapped by comparing the oxide abundances derived from Chang'E-1 Interference Imaging Spectrometer imagery and from Th contents inferred from Lunar Prospector to the geochemical indices. In terms of these results, we can get a new insight into the lithologic distribution on the Moon. Combination of Chang'E-3 data and other detector's information, Zhao *et al.*[3]. conducted a series of studies on the topography, geomorphology, composition, and stratigraphy of the Mon Rümker, and proposed two candidate sites with both the engineering constraints and scientific value for Chang'E-5 mission.

2.2 Lunar Surface Processes and Subsurface Structure

2.2.1 Space Weathering

By the new FeO map obtained by Chang'E-1 Imaging Interferometer (IIM), a compositional inhomogeneity across lunar highland regions was discovered. Also, mixing of highlands and mare regions was concluded on account of the compositional differences between those two terrains as well as the relationship between maturity effects and contents of FeO and TiO_2[4]. According to its remarkable effects on the interpretation of spectral data measured by the Visible-Near-Infrared Spectrometer (VNIS), the content of Submicroscopic Metallic iron (SMFe) and the Is/FeO maturity index of the lunar soil at the location of Chang'E-3 Yutu rover were measured before and after landing of the spacecraft. It has been proved that the most surface layer of lunar regolith which was removed by the rocket has a higher content of SMFe and is more weathered than that remained behind (Figure 2)[5].

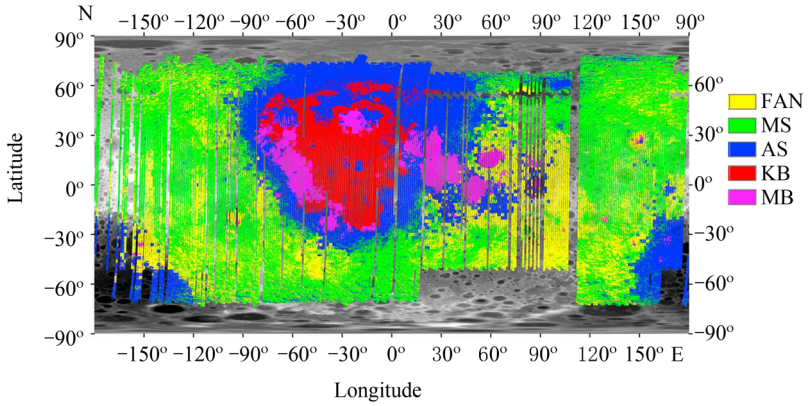


Fig. 1 Lithology maps of the lunar surface in a cylindrical projection with the pixel size 200 m. Distribution map of lunar rock suites across the Moon. The base image is LRO LOLA DEM data. The abbreviations FAN, AS, MS, MB, and KB in the legend refer to ferroan anorthosite, alkali suite, magnesian suite, mare basalt, and KREEP basalt, respectively

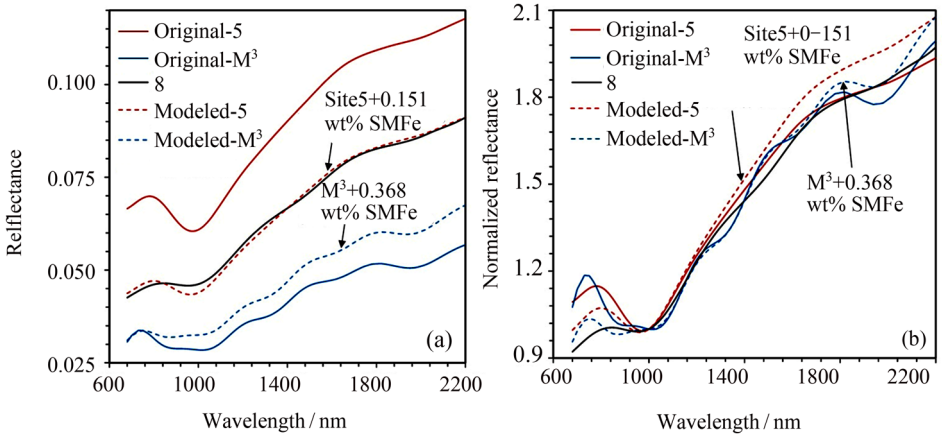


Fig. 2 Original (a) and normalized (b) spectra of the optimal modeling results. The SMFe abundance of the visually undisturbed soil, Site 8, is 0.368 wt% and that of the most-disturbed soil, Site 5, is 0.217 wt%. Those suggest that the maturity difference between Site 5 and Site 8 is a result of greater SMFe abundance in Site 8

2.2.2 Lunar Impact Crater Recognition and Volume Calculation

Craters are the most distinctive features on the lunar surface, and extracting craters from images and/or digital elevation models is one of the fundamental tasks in related research. Currently, craters are usually considered as circles in a planar view. Although this is the case in most cases, many craters display elliptical or even irregular shape. Liu *et al.*[6] proposed a dispersal crater detection algorithm based on a digital elevation model produced from the Chang'E-2 imagery and LRO laser altimeter data, in which the impact crater is treated as a closed basin structure. This algorithm can detect the real boundaries of an impact crater, and several morphological characteristics can be calculated based on the results.

Among these morphological characteristics, crater volume has important significance in understanding the impact cratering process. Wang *et al.*[7] devised an updated Black Top Hat (BTH) Transform function to quantify the volume of lunar impact craters on the Moon. The novelty of method is the iterative window sizes and slope factors based on which the volume can be calculated as the sum of the crater depth multiplied by the cell area with a higher accuracy. The algorithm was verified with the Chang'E DEM and LOLA DEM, achieving an overall relative accuracy of 95%.

2.2.3 Rock Fragments on the Surface and The Subsurface Structure

Rocks are widely distributed on the surface of the Moon, and its populations can provide important geological information related to the timing of critical events such as volcanism and meteorite bombardment. Using Navcam stereo images onboard the Yutu rover, Di *et al.*[8] identified and measured 582 rocks larger than 0.05 m in diameter. A simple exponential function exists in the statistical results of the size-frequency distribution, which is similar to the situation found in the landing area of Surveyor III (Figure 3).

On the study of lunar regolith, Di *et al.*[9] proposed an improved morphological method to determine the lunar regolith thickness by directly measuring the distance from the lunar ground surface to the floor (flat-bottomed and central-mound craters) or bench (concentric craters) of indicative small fresh craters. To accurately study the subsurface structure of the lunar surface, Lunar Penetrating Radar (LPR) was equipped on the Yutu rover. With the data acquired during CE-3 mission, Li *et al.*[10] analyzed the lunar regolith layer structure with the lunar regolith quantitative random model. Feng *et al.*[11] takes account of the heterogeneity of the regolith and derives regolith's permittivity distribution laterally and vertically to determine the thickness and structure of the lunar regolith. Their results indicate that this area is covered by relatively young, poorly layered deposits. Dong *et al.*[12] combined the data from penetrating radar and Panoramic Camera to calculate the lunar surface regolith parameters in Chang'E-3 landing area including its permittivity, density, weathered rate, conductivity and $FeO+TiO_2$ content. They found that the regolith growth rate is much faster than the previous estimation, and the regolith parameters are not uniform even in such a small study area. Lai *et al.*[13] analyzed the LPR data of 500 mHz frequency and speculated a model of the three-layered shallow structure with the top layer being weathered layer of ejecta blanket, the second layer being the ejecta blanket of the nearby impact crater, and the third layer being regarded as a mixture of stones and soil. Yuan *et al.*[14] built a three-dimensional geological model of the lunar subsurface structure with the high-frequency lunar penetrating radar data. They found more than five significant reflection horizons are evident in the LPR profile, which were interpreted as different period lava flow sequences deposited on the lunar surface.

2.2.4 Global Microwave Mapping

Chang'E microwave radiometer data is a unique source to study the lunar brightness temperatures and thermal emission behavior for the local lunar surface. Hu *et al.*[15] calibrated the Chang'E-2 Microwave Radiometer (MRM) by the analysis and simulation of Brightness Temperature (T_B) data and

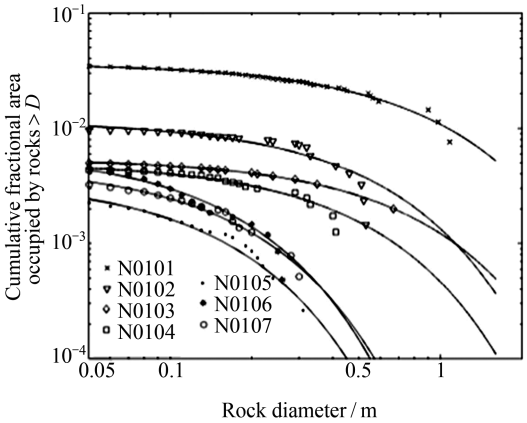


Fig. 3 Cumulative fractional area covered by rocks versus rock diameter at the Chang'E-3 site

by the relative comparison among the T_B and rock abundance and topography data. To improve the retrieval accuracy, they proposed two possible calibration sources[16]. Hu *et al.*[17] calibrated the data again, and compared the lunar TBs as measured by the Microwave RadioMeters (MRM) onboard Chang'E (Chang'E-1/2) with the historical data at the Apollo 15 and 17 landing sites (Figure 4)[17]. Also using the MRM data, the accurate and high-resolution lunar TB model was obtained by Cai and Lan[18]. The TB data also showed that the mafic lunar mare endured higher thermal regime than that of feldspathic highland in a lunar cycle[19]. A team from Jilin University also recalibrated the data, and used it for regional microwave thermal emission features of regional mare areas, like Mare Orientale and Tycho Crater[20]. The team also studied the Influence of ($FeO+TiO_2$) abundance on the microwave thermal emissions of lunar regolith. Comparisons between FTA and the CELMS data along Latitude 0° indicate that FTA strongly influences the MTE of the lunar regolith, even though the comparison along Longitude 0° indicates that FTA is not the decisive factor[21].

3 Asteroid Exploration

Based on the high spatial resolution images obtained by Chang'E-2 spacecraft, two new topographic characteristics are revealed, one is a connection region with a particular spectral value locating at the corner of the large lobe, and the other is an object seeming like a fixed star at the background of the images[22]. Also, a new Toutatis' radar 3D topography model with the constraint of Chang'E-2 optical images was obtained by Zhao *et al.*[23].

4 Moon-based Observations by Chang'E-3

4.1 Moon-based EUV Observations

An Extreme Ultraviolet (EUV) telescope called EUV Camera (EUVC) was installed on the lunar lander of Chang'E-3. It can take instantaneous images of the Earth's plasmasphere through 30.4 nm EUV wavelength band. The dense cold plasmas in the plasmasphere are confined by the geomagnetic field, in which the He^+ ions can scatter the 30.4 nm photons from the sunlight. The EUVC captures these scattered 30.4 nm photons *via* its imaging detector and yields images of the plasmasphere. Owing to the moon-based viewpoint, EUVC can take the global and side view (meridian view) of the plasmasphere. Because the distance between the Earth and the Moon is about 60 Earth radii (R_e), the field of view (FOV) of the EUVC images can be as large as $15\,R_e \times 15\,R_e$, which well encloses the outer boundary (called plasmapause) of the plasmasphere[24−26].

The EUVC can take one image of the plasmasphere every 10 minutes. The pixel size of the EUVC images is 150×150 ($0.1\,R_e$/pixel). The continuously observed time series images of EUVC form movies of the plasmasphere, which display dynamic evolutions of the plasmasphere as responses to the geomagnetic activities and substorms. The working period of the EUVC on the Moon is from December 2013 to June 2014. The accumulated observing time of EUVC is

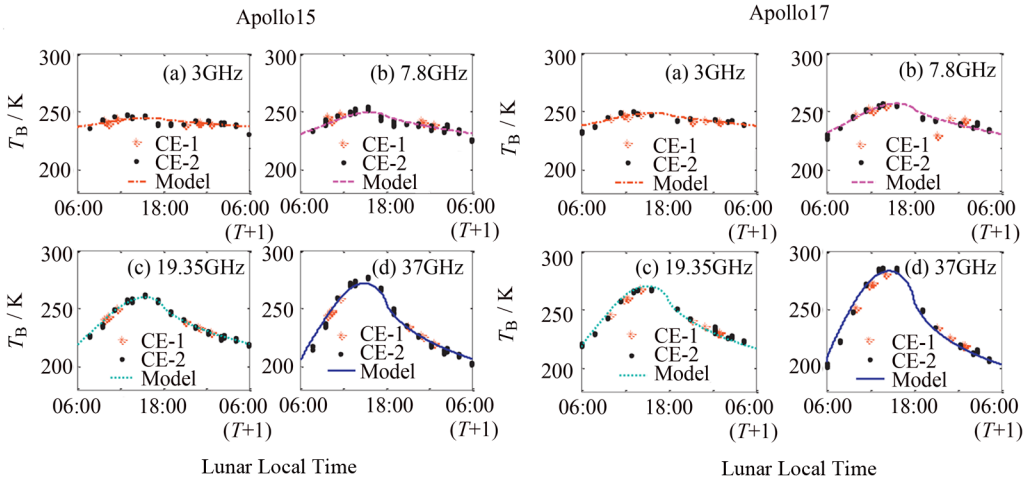


Fig. 4 Modified observational T_B variations against lunar local time. The curves represent the simulated TBs based on the retrieved parameters from in-situ experiments

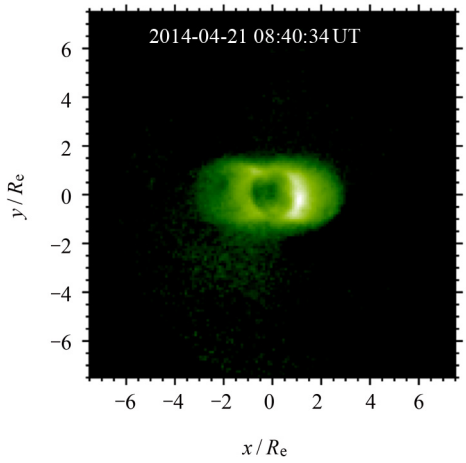


Fig. 5 A sample image of the plasmasphere observed by EUVC

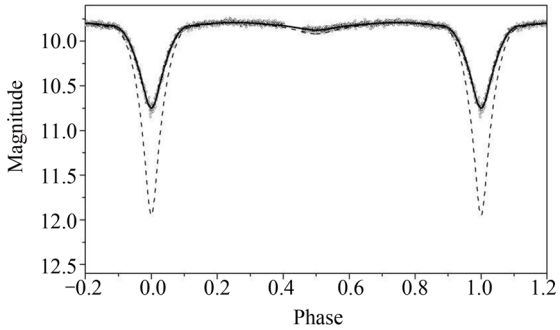


Fig. 6 Light curve of V548 Cygni observed on 2014 May 13–14 with LUT (open circles). The solid line refers to the theoretical light curve with the third light, while the dashed line refers to the theoretical light curve without the third light but with the same photometric parameters

about 230 hours, in which EUVC obtained 388 scientific images in total. A sample image of the plasmasphere observed by EUVC is shown in Figure 5[26]. Most of the images were taken just before the sunset on the Moon to minimize the contamination of the direct sunlight to the plasmasphere images[25,26].

Since the images taken by EUVC are the global and side view of the plasmasphere, the plasmapause positions can be derived from the EUVC images directly. Meanwhile, the plasmapause locations can also be determined from the in-situ data of the satellites running at the near-Earth orbits. The comparison between the plasmapause position values derived from the EUVC images and in-situ measurements shows excellent agreement, which demonstrated the reliability of the EUVC images as well as the advantages of Moon-based observation for plasmasphere[24].

The configuration of the plasmasphere may change dramatically during substorms. On 20 April 2014, the magnetosphere of the Earth was impacted by a Coronal Mass Ejection (CME) and several substorms were recorded by the ground geomagnetic stations. The simultaneous time-series images of the plasmasphere during the substorms were observed by EUVC, which revealed dynamic variations of the plasmasphere as the responses to the substorms. The analysis of these time series EUVC images shows that a substorm causes a local inflation of the plasmasphere (in contrast to erosions associated with geomagnetic storms) on the nightside of the Earth and leads to a bulge at the nightside of the plasmasphere, which in turn corotates with the Earth and appears at the dayside of the plasmasphere. In the observing period of EUVC (20–22 April 2014), three bulges were recorded by the EUVC images, which correspond to the three substorms shown in the AE-index data of the ground geomagnetic stations[26].

4.2 Moon-base Astronomical Observations

The Lunar-based Ultraviolet Telescope (LUT) is the first robotic astronomical telescope deployed on the Moon surface sent by the Chang'E-3 mission. It is very useful to monitor close binaries continuously and uninterruptedly because of the slow rotation of the Moon. Complete light curves of binary stars in the UV-band could be obtained at the same time. In the time interval from 2014 to 2015, several close binaries (*e.g.*, V548 Cyg, V921 Her, AI Dra, TW Dra) were observed since they are ideal targets to investigate some astrophysical problems[27−30]. Their UV light curves were analyzed comprehensively by researchers at the group of Binaries and Variable stars in Yunnan Observatories.

It is shown that three binary systems, V548 Cyg, AI Dra and TW Dra are semi-detached binary systems[27−29], while V921 Her is a marginal contact binary[30]. The three binaries stay at an interesting evolutionary stage where the secondary stars fill the critical Roche lobe transferring mass to the primary stars. These properties are in agreement with the continuously increasing in their orbital periods[27−29]. All of the four targets are accompanied by tertiary or even more component stars[27−30]. For example, a large quantity of third light in V548 Cyg was detected by two different ways, *i.e.* the light curve analysis[27] and O-C diagram investigation. It is proposed that the presence of the additional components may have played an important role for the origin and evolution of the central close binaries by removing

angular momentum during the early dynamical interaction and late evolution. The existent additional companions orbiting these typical semi-detached or marginal-contact binaries make them very interesting targets to study in the future (Figure 6).

Acknowledgements We thank Di Kaichang, Xiao Long, Ping Jingsong, Li Xiongyao, Li Yang, Wang Huaning, He Han, Qian Shengbang, Zhu Liying, Liao Wenping and Zhou Xiao for their help with the manuscript.

References

[1] WANG X M, ZHANG X B, WU K. Thorium distribution on the lunar surface observed by Chang'E-2 gamma-ray spectrometer [J]. *Astrophys. Space Sci.*, 2016, **361**(7): 234

[2] WANG X M, ZHAO S Y. New insights into lithology distribution across the Moon [J]. *J. Geophys. Res.: Planets*, 2017, **122**(10): 2034-2052

[3] ZHAO J N, XIAO L, QIAO L, *et al.* The Mons Rumker volcanic complex of the Moon: a candidate landing site for the Chang'E-5 mission [J]. *J. Geophys. Res.: Planets*, 2017, **122**(7): 1419-1442

[4] SUN L Z, LING Z C, ZHANG J, *et al.* Lunar iron and optical maturity mapping: results from partial least squares modeling of Chang'E-1 IIM data [J]. *Icarus*, 2016, **280**: 183-198

[5] WANG Z C, WU Y Z, BLEWETT D T, *et al.* Submicroscopic metallic iron in lunar soils estimated from the in situ spectra of the Chang'E-3 mission [J]. *Geophys. Res. Lett.*, 2017, **44**(8): 3485-3492

[6] LIU D Y, CHEN M, QIAN K J, *et al.* Boundary detection of dispersal impact craters based on morphological characteristics using lunar digital elevation model [J]. *IEEE J. Selec. Top. Appl. Earth Observ. Remote Sens.*, 2017, **10**(12): 5632-5646

[7] WANG J, CHENG W M, LUO W, *et al.* An iterative black top hat transform algorithm for the volume estimation of lunar impact craters [J]. *Remote Sens.*, 2017, **9**(9): 952

[8] DI K C, XU B, PENG M, *et al.* Rock size-frequency distribution analysis at the Chang'E-3 landing site [J]. *Planet. Space Sci.*, 2016, **120**: 103-112

[9] DI K C, SUN S J, YUE Z Y, *et al.* Lunar regolith thickness determination from 3D morphology of small fresh craters [J]. *Icarus*, 2016, **267**: 12-23

[10] LI J, ZENG Z F, LIU C, *et al.* A Study on lunar regolith quantitative random model and lunar penetrating radar parameter inversion [J]. *IEEE Geosci. Remote Sens. Lett.*, 2017, **14**(11): 1953-1957

[11] FENG J Q, SU Y, DING C Y, *et al.* Dielectric properties estimation of the lunar regolith at CE-3 landing site using lunar penetrating radar data [J]. *Icarus*, 2017, **284**: 424-430

[12] DONG Z H, FANG G Y, JI Y C, *et al.* Parameters and structure of lunar regolith in Chang'E-3 landing area from Lunar Penetrating Radar (LPR) data [J]. *Icarus*, 2017, **282**: 40-46

[13] LAI J L, XU Y, ZHANG X P, *et al.* Structural analysis of lunar subsurface with Chang'E-3 lunar penetrating radar [J]. *Planet. Space Sci.*, 2016, **120**: 96-102

[14] YUAN Y F, ZHU P M, ZHAO N, *et al.* The 3-D geological model around Chang'E-3 landing site based on lunar penetrating radar Channel 1 data [J]. *Geophys. Res. Lett.*, 2017, **44**(13): 6553-6561

[15] HU G P, ZHENG Y C, XU A A, *et al.* Qualitative verification of CE-2's Microwave measurement: relative calibration based on brightness temperature model and data fusion [J]. *IEEE Trans. Geosci. Remote Sens.*, 2016, **54**(3): 1598-1609

[16] HU G P, ZHENG Y C, XU A A, *et al.* Microwave brightness temperature of the Moon: the possibility of setting a calibration source of the lunar surface [J]. *IEEE Geosci. Remote Sens. Lett.*, 2016, **13**(2): 182-186

[17] HU G P, CHAN K L, ZHENG Y C, *et al.* Comparison and evaluation of the Chang'E microwave radiometer data based on theoretical computation of brightness temperatures at the Apollo 15 and 17 sites [J]. *Icarus*, 2017, **294**: 72-80

[18] CAI Z C, LAN T. Lunar brightness temperature model based on the microwave radiometer data of Chang'E-2 [J]. *IEEE Trans. Geosci. Remote Sens.*, 2017, **55**(10): 5944-5955

[19] WEI G F, LI X Y, WANG S J. Inversions of subsurface temperature and thermal diffusivity on the Moon based on high frequency of Chang'E-1 microwave radiometer data [J]. *Icarus*, 2016, **275**: 97-106

[20] MENG Z G, ZHANG J D, CAI Z C, *et al.* Microwave thermal emission at tycho area and its geological significance [J]. *IEEE J. Selected Top. Appl. Earth Observ. Remote Sens.*, 2017, **10**(6): 2984-2990

[21] MENG Z G, YANG G D, PING J S, *et al.* Influence of ($FeO+TiO_2$) abundance on the microwave thermal emissions of lunar regolith [J]. *Sci. China: Earth Sci.*, 2016, **59**(7): 1498-1507

[22] ZHENG C, PING J S, WANG M Y. Hierarchical classification for the topography analysis of Asteroid (4179) Toutatis from the Chang'E-2 images [J]. *Icarus*, 2016, **278**: 119-127

[23] ZHAO W, XIAO T, LIU P, *et al.* Radar model fusion of asteroid (4179) Toutatis via its optical images observed by Chang'E-2 probe [J]. *Planet. Space Sci.*, 2016, **125**: 87-95

[24] HE F, ZHANG X X, CHEN B, *et al.* Determination of the Earth's plasmapause location from the CE-3 EUVC images [J]. *J. Geophys. Res.: Space Phys.*, 2016, **121**(1): 296-304

[25] YAN Y, WANG H N, HE H. Analysis of observational data from extreme Ultra-Violet camera onboard Chang'E-3 mission [J]. *Astrophys. Space Sci.*, 2016, **361**(2): 76

[26] HE H, SHEN C, WANG H N, *et al.* Response of plasmaspheric configuration to substorms revealed by Chang'E-3 [J]. *Sci. Rep.*, 2016, **6**: 32362

[27] ZHU L Y, ZHOU X, HU J Y, *et al.* LUT reveals an algol-type eclipsing binary with three additional stellar companions in a multiple system [J]. *Astron. J.*, 2016, **151**(4): 107

[28] LIAO W P, QIAN S B, LI L J, *et al.* LUT observations of the mass-transferring binary AI Dra [J]. *Astrophys. Space Sci.*, 2016, **361**(6): 184

[29] LIAO W P, QIAN S B, ZEJDA M, *et al.* Lunar-based ultraviolet telescope study of the well-known Algol-type binary TW Dra [J]. *Res. Astron. Astrophys.*, 2016, **16**(6): 9

[30] ZHOU X, QIAN S B, ZHANG J, *et al.* The photometric investigation of v921 her using the Lunar-Based ultraviolet telescope of Chang'E-3 mission [J]. *Adv. Astron.*, 2016: 746897